A&A 574, A27 (2015)
DOI: 10.1051/0004-6361/201322694

Astronomy & Astrophysics

Probing the gamma-ray emission from HESS J1834–087 using H.E.S.S. and *Fermi* LAT observations

H.E.S.S. Collaboration: A. Abramowski[1], F. Aharonian[2,3,4], F. Ait Benkhali[2], A. G. Akhperjanian[5,4], E. Angüner[6], G. Anton[7], M. Backes[8], S. Balenderan[9], A. Balzer[10,11], A. Barnacka[12], Y. Becherini[13], J. Becker Tjus[14], K. Bernlöhr[2,6], E. Birsin[6], E. Bissaldi[15], J. Biteau[16,17], M. Böttcher[18], C. Boisson[19], J. Bolmont[20], P. Bordas[21], J. Brucker[7], F. Brun[2], P. Brun[22], T. Bulik[23], S. Carrigan[2], S. Casanova[18,2], P. M. Chadwick[9], R. Chalme-Calvet[20], R. C. G. Chaves[22], A. Cheesebrough[9], M. Chrétien[20], S. Colafrancesco[24], G. Cologna[25], J. Conrad[26,27], C. Couturier[20], Y. Cui[21], M. Dalton[28,29], M. K. Daniel[9], I. D. Davids[18,8], B. Degrange[16], C. Deil[2], P. deWilt[30], H. J. Dickinson[26], A. Djannati-Ataï[31], W. Domainko[2], L. O'C. Drury[3], G. Dubus[32], K. Dutson[33], J. Dyks[12], M. Dyrda[34], T. Edwards[2], K. Egberts[15], P. Eger[2], P. Espigat[31], C. Farnier[26], S. Fegan[16], F. Feinstein[35], M. V. Fernandes[1], D. Fernandez[35], A. Fiasson[36], G. Fontaine[16], A. Förster[2], M. Füßling[11], M. Gajdus[6], Y. A. Gallant[35], T. Garrigoux[20], G. Giavitto[10], B. Giebels[16], J. F. Glicenstein[22], M.-H. Grondin[2,25,⋆], M. Grudzińska[23], S. Häffner[7], J. Hahn[2], J. Harris[9], G. Heinzelmann[1], G. Henri[32], G. Hermann[2], O. Hervet[19], A. Hillert[2], J. A. Hinton[33], W. Hofmann[2], P. Hofverberg[2], M. Holler[11], D. Horns[1], A. Jacholkowska[20], C. Jahn[7], M. Jamrozy[37], M. Janiak[12], F. Jankowsky[25], I. Jung[7], M. A. Kastendieck[1], K. Katarzyński[38], U. Katz[7], S. Kaufmann[25], B. Khélifi[31], M. Kieffer[20], S. Klepser[10], D. Klochkov[21], W. Kluźniak[12], T. Kneiske[1], D. Kolitzus[15], Nu. Komin[36], K. Kosack[22], S. Krakau[14], F. Krayzel[36], P. P. Krüger[18,2], H. Laffon[28], G. Lamanna[36], J. Lefaucheur[31], A. Lemière[31], M. Lemoine-Goumard[28], J.-P. Lenain[20], T. Lohse[6], A. Lopatin[7], C.-C. Lu[2], V. Marandon[2], A. Marcowith[35], R. Marx[2], G. Maurin[36], N. Maxted[30], M. Mayer[11], T. J. L. McComb[9], J. Méhault[28,29,⋆], P. J. Meintjes[39], U. Menzler[14], M. Meyer[26], R. Moderski[12], M. Mohamed[25], E. Moulin[22], T. Murach[6], C. L. Naumann[20], M. de Naurois[16], J. Niemiec[34], S. J. Nolan[9], L. Oakes[6], H. Odaka[2], S. Ohm[33], E. de Oña Wilhelmi[2], B. Opitz[1], M. Ostrowski[37], I. Oya[6], M. Panter[2], R. D. Parsons[2], M. Paz Arribas[6], N. W. Pekeur[18], G. Pelletier[32], J. Perez[15], P.-O. Petrucci[32], B. Peyaud[22], S. Pita[31], H. Poon[2], G. Pühlhofer[21], M. Punch[31], A. Quirrenbach[25], S. Raab[7], M. Raue[1], I. Reichardt[31], A. Reimer[15], O. Reimer[15], M. Renaud[35], R. de los Reyes[2], F. Rieger[2], L. Rob[40], C. Romoli[3], S. Rosier-Lees[36], G. Rowell[30], B. Rudak[12], C. B. Rulten[19], V. Sahakian[5,4], D. A. Sanchez[36], A. Santangelo[21], R. Schlickeiser[14], F. Schüssler[22], A. Schulz[10], U. Schwanke[6], S. Schwarzburg[21], S. Schwemmer[25], H. Sol[19], G. Spengler[6], F. Spies[1], Ł. Stawarz[37], R. Steenkamp[8], C. Stegmann[11,10], F. Stinzing[7], K. Stycz[10], I. Sushch[6,18], J.-P. Tavernet[20], T. Tavernier[31], A. M. Taylor[3], R. Terrier[31], M. Tluczykont[1], C. Trichard[36], K. Valerius[7], C. van Eldik[7], B. van Soelen[39], G. Vasileiadis[35], C. Venter[18], A. Viana[2], P. Vincent[20], H. J. Völk[2], F. Volpe[2], M. Vorster[18], T. Vuillaume[32], S. J. Wagner[25], P. Wagner[6], R. M. Wagner[26], M. Ward[9], M. Weidinger[14], Q. Weitzel[2], R. White[33], A. Wierzcholska[37], P. Willmann[7], A. Wörnlein[7], D. Wouters[22], R. Yang[2], V. Zabalza[2,33], M. Zacharias[14], A. A. Zdziarski[12], A. Zech[19], H.-S. Zechlin[1].
From *Fermi*-LAT Collaboration: F. Acero[41], J. M. Casandjian[41], J. Cohen-Tanugi[35], F. Giordano[42,43], L. Guillemot[44], J. Lande[45], H. Pletsch[46,47], and Y. Uchiyama[48]

(Affiliations can be found after the references)

Received 17 September 2013 / Accepted 22 June 2014

ABSTRACT

Aims. Previous observations with the High Energy Stereoscopic System (H.E.S.S.) have revealed an extended very-high-energy (VHE; $E >$ 100 GeV) γ-ray source, HESS J1834−087, coincident with the supernova remnant (SNR) W41. The origin of the γ-ray emission was investigated in more detail with the H.E.S.S. array and the Large Area Telescope (LAT) onboard the *Fermi* Gamma-ray Space Telescope.

Methods. The γ-ray data provided by 61 h of observations with H.E.S.S., and four years with the *Fermi* LAT were analyzed, covering over five decades in energy from 1.8 GeV up to 30 TeV. The morphology and spectrum of the TeV and GeV sources were studied and multiwavelength data were used to investigate the origin of the γ-ray emission toward W41.

Results. The TeV source can be modeled with a sum of two components: one point-like and one significantly extended ($\sigma_{\rm TeV} = 0.17^\circ \pm 0.01^\circ$), both centered on SNR W41 and exhibiting spectra described by a power law with index $\Gamma_{\rm TeV} \simeq 2.6$. The GeV source detected with *Fermi* LAT is extended ($\sigma_{\rm GeV} = 0.15^\circ \pm 0.03^\circ$) and morphologically matches the VHE emission. Its spectrum can be described by a power-law model with an index $\Gamma_{\rm GeV} = 2.15 \pm 0.12$ and smoothly joins the spectrum of the whole TeV source. A break appears in the γ-ray spectra around 100 GeV. No pulsations were found in the GeV range.

Conclusions. Two main scenarios are proposed to explain the observed emission: a pulsar wind nebula (PWN) or the interaction of SNR W41 with an associated molecular cloud. X-ray observations suggest the presence of a point-like source (a pulsar candidate) near the center of the remnant and nonthermal X-ray diffuse emission that could arise from the possibly associated PWN. The PWN scenario is supported by the compatible positions of the TeV and GeV sources with the putative pulsar. However, the spectral energy distribution from radio to γ-rays is reproduced by a one-zone leptonic model only if an excess of low-energy electrons is injected following a Maxwellian distribution by a pulsar with a high spin-down power ($>10^{37}$ erg s^{-1}). This additional low-energy component is not needed if we consider that the point-like TeV source is unrelated to the extended GeV and TeV sources. The interacting SNR scenario is supported by the spatial coincidence between the γ-ray sources, the detection of OH (1720 MHz) maser lines, and the hadronic modeling.

Key words. acceleration of particles – ISM: supernova remnants – ISM: clouds – cosmic rays

⋆ Corresponding authors: J. Méhault, e-mail: mehault@cenbg.in2p3.fr; M.-H. Grondin, e-mail: grondin@cenbg.in2p3.fr

1. Introduction

During the 2005–2006 Galactic Plane Survey in the very-high-energy (VHE; $E > 100$ GeV) range, the High Energy Stereoscopic System (H.E.S.S.), an array of imaging atmospheric Cherenkov telescopes, revealed more than a dozen new sources (Aharonian et al. 2005a, 2006b). Extensions of the survey and deeper observations of the Galactic plane led to the detection of more than 80 sources (Carrigan et al. 2013). While many Galactic TeV γ-ray sources can be identified with counterparts at other wavelengths, such as the binary LS 5039 (Aharonian et al. 2005b, 2006c), the supernova remnant (SNR) RX J1713−3946 (Aharonian et al. 2004), or HESS J1356−645 (Abramowski et al. 2011), associated with a pulsar wind nebula (PWN), more than 20 γ-ray sources remain unidentified to date. Pulsar wind nebulae are the dominant class of Galactic TeV sources with at least 27 identifications up to now out of a total of more than 35 sources considered to be potentially due to PWN emission. The presence of an energetic pulsar close to the position of the source is an important clue in the identification process.

HESS J1834−087 is one such unidentified source (Aharonian et al. 2006b) that was later detected by the MAGIC telescope (Albert et al. 2006). It features bright and extended (intrinsic Gaussian width $\sigma = 0.2°$) VHE emission spatially coincident with the SNR G23.3−0.3 (W41). Additionally, high-energy (HE; $E > 100$ MeV) emission spatially coincident with W41 was detected with the *Fermi* Large Area Telescope (LAT) and listed in the first- and second-year catalogs as 1FGL J1834.3−0842c (Abdo et al. 2010a) and 2FGL J1834.3−0848 (Nolan et al. 2012).

The SNR W41 shows an incomplete shell of ∼33′ diameter in the radio domain (Tian et al. 2007). Several HII regions are spatially coincident with the shell but unrelated to the remnant as explained by Leahy et al. (2008), who also estimated the kinematic distance of W41 to be between 3.9 and 4.5 kpc based on HI and CO observations. The associated cloud has a radial velocity in the local standard of rest (lsr) of $V_{Cl_{\rm lsr}} = 77$ km s^{-1}. Frail et al. (2013) detected OH (1720 MHz) maser line emission, which demonstrates the physical association between the SNR and the molecular cloud (MC). The maser is located near the center of the remnant, and its radial velocity ($V_{\rm OH_{lsr}} \simeq 74$ km s^{-1}) coincides with the MC velocity. Tian et al. (2007) estimated the ambient density $n \sim 6$ cm^{-3}, and, by applying a Sedov model (Cox 1972), derived an age of 6×10^4 yr. However, the observed radius of the shock front is larger than the radius of the shell merged with the surrounding medium (called complete cooling in Cox 1972). The age determined by Tian et al. (2007) assuming a rapid cooling of the blast wave and a completed shell formation is $\sim 2 \times 10^5$ yr.

With the *XMM-Newton* observatory, Mukherjee et al. (2009) detected a central compact object (CCO; XMMU J183435.3−084443) at the center of the remnant ($l = 23.236°, b = -0.270°$) in X-rays, as well as a faint tail-like emission. The spectral parameters of this diffuse emission, which could be a PWN, were extracted in a region of 0.1° radius. The integrated energy flux and the spectral index are $F_{2-10\ \rm keV} = (4.2 \pm 2.2) \times 10^{-13}$ erg cm^{-2} s^{-1} and $\Gamma = 1.9 \pm 1.0$. Perhaps because of a better resolution than available with the European Photon Imaging Camera (EPIC) onboard *XMM-Newton* and a short observation time (∼40 ks), Misanovic et al. (2011) did not report the offset emission in *Chandra* data but a compact nonthermal X-ray nebula surrounding the CCO (CXOU J183434.9−084443), which could be a dust halo or a PWN. Despite the nondetection of X-ray pulsations from the CCO, the existence of the nonthermal X-ray nebula suggests that the compact object could be a pulsar.

No radio emission from the putative pulsar or its nebula has been detected so far. Radio upper limits were derived from the Very Large Array (VLA) observations at 20 cm (Helfand et al. 2006) and the 1.1 mm Bolocam (Aguirre et al. 2011) Galactic Plane Survey images within a 0.1° radius around the position of the point-like X-ray source.

Two scenarios have been proposed to explain the TeV emission: the interaction between the SNR W41 and a nearby MC (Li & Chen 2012; Castro et al. 2013) and a PWN powered by the compact object CXOU J183434.9−084443 (Misanovic et al. 2011).

The analyses presented here were performed using data taken with the H.E.S.S. telescopes and *Fermi* LAT. H.E.S.S. is an array of four identical 13 m diameter imaging telescopes located in the Khomas Highland of Namibia at an altitude of 1800 m. A larger telescope with 28 m diameter (H.E.S.S. Phase II) has been built in the center of the array and saw its first light in July 2012. No data from H.E.S.S. Phase II were used in this work. H.E.S.S. is sensitive to γ-rays at energies above 100 GeV up to several tens of TeV and has a large field-of-view (FoV) of 5° diameter. Requiring at least two telescopes triggered by an air shower, the system yields a very good angular resolution ($r_{68\%} \sim 0.1°$), energy resolution ($\Delta E/E \sim 15\%$), and an efficient background rejection (Aharonian et al. 2006a). These characteristics, together with its geographic location, make H.E.S.S. ideally suited for discoveries and studies of extended sources in the Galactic plane.

The LAT onboard the *Fermi* Gamma-ray Space Telescope, launched in June 2008, is a pair-conversion telescope sensitive to photons in a broad energy band from ∼20 MeV to more than 300 GeV. It has a wide FoV of 2.4 sr and a good angular resolution ($r_{68\%} \lesssim 1°$ above 1 GeV). For a detailed description of the instrument, see Atwood et al. (2009).

Deeper observations of the region of SNR W41 with H.E.S.S. and *Fermi* LAT since the discovery of the γ-ray source allow morphological and spectral analyses over a very wide energy range of a few GeV to several tens of TeV, providing new insights into the origin of the γ-ray emission coincident with SNR W41.

The H.E.S.S. observations, data analysis, and characteristics of HESS J1834−087 are provided in Sect. 2, while the results from the analysis of the *Fermi* LAT data are presented in Sect. 3. A discussion on possible γ-ray emission mechanisms is given in Sect. 4.

2. H.E.S.S. observations and data analysis

H.E.S.S. observations of 28 min duration were taken in wobble mode centered on the position of the SNR W41. The pointing alternates between offsets of ±0.5° in declination and right ascension with respect to the nominal target position. After standard quality selection (Aharonian et al. 2006a) to remove data affected by unstable weather conditions or hardware-related problems, the total live-time of the data set, including data presented in the discovery paper (Aharonian et al. 2006b), is 61 h. The zenith angle of the observations ranges from 10° to 45°, with a median value of 20°.

The data were analyzed with the Model Analysis method, implemented in the ParisAnalysis software (version 0-8-22), which compares the raw atmospheric shower images in the Cherenkov camera with the prediction of a semi-analytical

Table 1. Centroid (Galactic coordinates) and extension fits to the H.E.S.S. events spatial distribution in the W41 region.

	Model tested	TS	$S_{\rm improv}{}^{a}$	$N_{\rm par}{}^{b}$	l [°]	b [°]	σ [°]^{c}
(*A*)	Point-like	–	–	3	23.222 ± 0.004	−0.268 ± 0.004	–
(*B*)	Gaussian	566.4	23.8	4	23.22 ± 0.01	−0.31 ± 0.01	0.15 ± 0.01
	Point-like				23.23 ± 0.01	−0.26 ± 0.01	–
(*C*)	+	31.6	5.0	7			
	Gaussian				23.22 ± 0.01	−0.32 ± 0.01	0.17 ± 0.01

Notes. The errors given are statistical only. The test statistic (TS; defined in Sect. 3.2) quantifies the improvement of a model to a more complex one. [(a)] Significance of the improvement for each of the alternative models with respect to the previous less complex model. [(b)] Number of free parameters. [(c)] σ is the intrinsic size of the source, i.e., PSF-substracted.

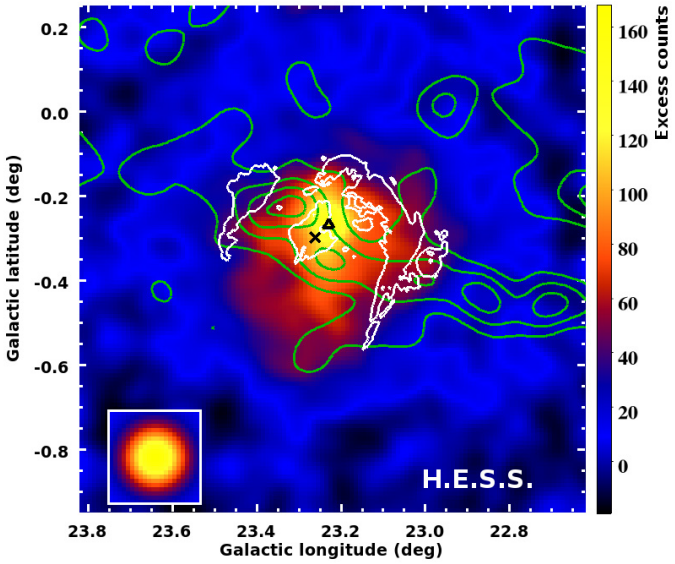

Fig. 1. H.E.S.S. image of the VHE γ-ray excess in the direction of SNR W41 after standard cut analysis. The image was smoothed with a Gaussian kernel of 0.068° corresponding to the instrument's point-spread function for this data set, which is shown in the inset. Green contours represent the GRS ^{13}CO data around W41 integrated in the velocity range 74 km s^{-1} to 82 km s^{-1} and smoothed with the same kernel. White contours of the VLA radio data at 20 cm show the shell-type SNR. The position of CXOU J183434.9−084443 and the brightest OH (1720 MHz) maser are indicated with a triangle and a cross, respectively. The linear color scale is in units of counts per smoothing Gaussian width.

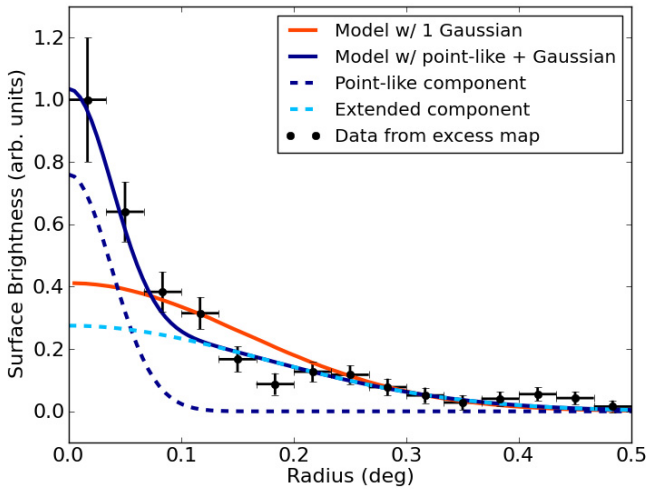

Fig. 2. H.E.S.S. radial profile of the uncorrelated excess map centered on the position of the putative pulsar. The solid dark blue line shows the result of the best-fit model (labeled (C) in Table 1) estimated in Sect. 2.1. The dark blue and light blue dashed lines represent the point-like and Gaussian components of this model. The profile from the single Gaussian model (labeled (B) in Table 1) is plotted in orange.

model (de Naurois & Rolland 2009). Two different event selection cuts were applied. Standard cuts, which require a minimum intensity in the camera image of 60 photo-electrons (p.e.), were used to compute energy spectra and sky maps. To improve the angular resolution and obtain better background rejection, hard cuts (higher minimum intensity of 120 p.e.) were used for morphological studies. The energy thresholds for standard and hard cuts are 177 GeV and 217 GeV, respectively. A second analysis (HAP, Aharonian et al. 2006a), which included independent calibration of pixel amplitude and event reconstructions and discrimination based on Hillas moments of the cleaned shower image, was used for cross-checks and provides compatible results.

2.1. Morphological analysis

Figure 1 presents the H.E.S.S. excess map obtained after the analysis with standard cuts and smoothed with a Gaussian kernel of 0.068°, which corresponds to the mean point-spread function (PSF) for this data set. Cloud density traced by ^{13}CO from the Galactic Ring Survey (GRS; Jackson et al. 2006) smoothed with the same Gaussian kernel, radio 20 cm contours (White et al. 2005) from W41, and the position of the CCO CXOU J183434.9−084443 are shown as well.

The detection of the TeV source is clear, with a significance of $\simeq 27\sigma$ within an integration radius of 0.3° centered on the candidate pulsar position. The following morphological results were obtained with the tools included in the ParisAnalysis software. The best-fit position assuming a point-like model (model (A) in Table 1) can be considered compatible with the pulsar position (0.01° away from it). Using a symmetrical Gaussian model (model (B) in Table 1) significantly improves the likelihood of the fit with respect to the previous model. The best-fit position moves 0.04° away from the putative pulsar but is still compatible with it. The sum of a point-like and a symmetrical Gaussian convolved with the PSF (model (C) in Table 1) again improves (5σ) the fit with respect to the single-Gaussian model. No significant extension of the central component was found. As can be seen in Fig. 2, the radial profiles of the unsmoothed best-fit model (model (C)) and the excess map centered on the position of the putative pulsar agree well. For comparison, the radial profile of the single-Gaussian model (model (B)) is displayed. Table 1 summarizes the tested models and Fig. 4 represents the best-fit morphology.

The wide energy range covered by H.E.S.S. allows a morphological study in two energy bands: we used data below and

Table 2. H.E.S.S. best-fit spectral parameters assuming a power-law model (Eq. (1)) between 0.2 and 30 TeV.

Region	$\Phi(E_{\rm dec})$ $\times 10^{-12}$ [cm^{-2} s^{-1} TeV^{-1}]	$E_{\rm dec}$ [TeV]	Γ	Equivalent χ^2/ndf	$I_{1-30\ \rm TeV}$ $\times 10^{-12}$ [ph cm^{-2} s^{-1}]
Central	$2.28 \pm 0.15_{\rm stat}$	0.633	$2.67 \pm 0.11_{\rm stat}$	22/18	$0.40 \pm 0.05_{\rm stat}$
Annular	$4.33 \pm 0.22_{\rm stat}$	0.716	$2.60 \pm 0.07_{\rm stat}$	37/32	$1.13 \pm 0.11_{\rm stat}$
Total	$6.50 \pm 0.27_{\rm stat}$	0.687	$2.64 \pm 0.06_{\rm stat}$	29/32	$1.46 \pm 0.11_{\rm stat}$

Notes. The systematic errors are conservatively estimated to be ±0.2 on the photon index and 20% on the flux (Aharonian et al. 2006a).

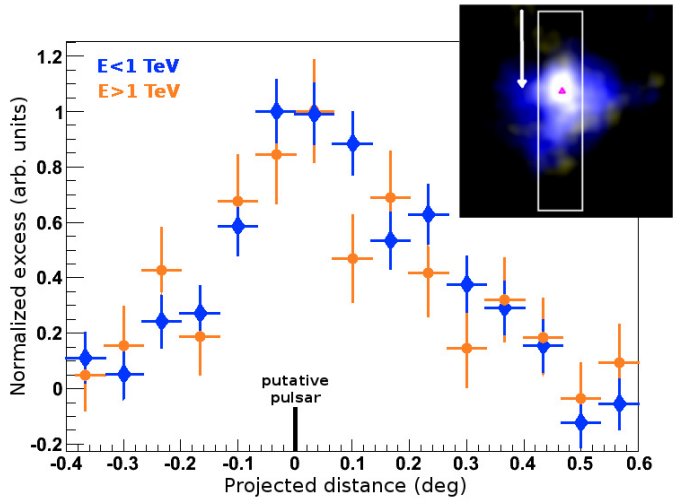

Fig. 3. H.E.S.S. slices in the uncorrelated excess map along the direction perpendicular to the Galactic plane (white arrow in the inset) in two independent energy bands (E < 1 TeV: blue and E > 1 TeV: orange). The slices are centered on the candidate pulsar position (marked by a triangle in the inset). The composite color image (inset) shows the box (height = 1.0°, width = 0.22°) used for the profile.

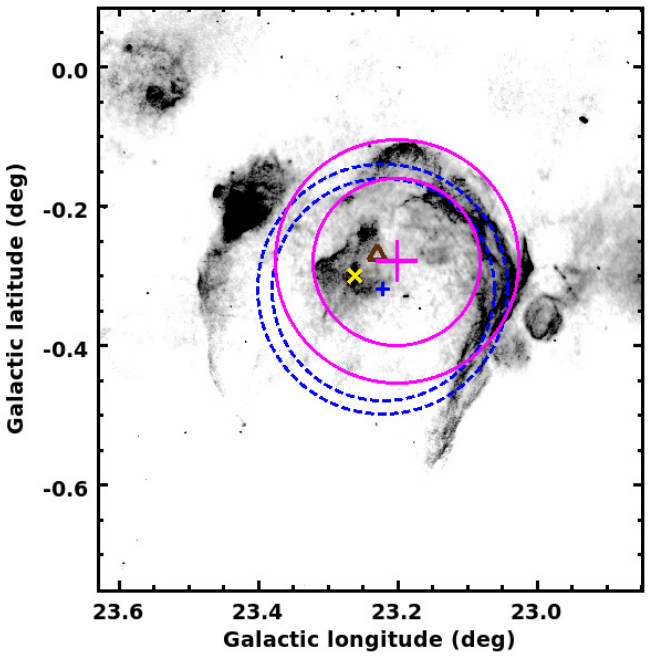

Fig. 4. 20 cm radio continuum map (Helfand et al. 2006) with superimposed best-fit positions as vertical crosses (their sizes indicate the statistical errors) and intrinsic extensions as rings. Magenta and dashed blue represent the Gaussian model of the *Fermi* LAT source and the extended component of the two-component model of the H.E.S.S. source. The inner and outer radius represents ±1σ errors on the fitted extension. The candidate pulsar (triangle, brown) and OH maser (cross, yellow) positions are also reported.

above 1 TeV to obtain equivalent statistics in each band. Slices perpendicular to the Galactic plane do not show any significant variation of the morphology, as seen in Fig. 3. The same conclusion was obtained along other angles. The corresponding composite image (Fig. 3, inset) highlights that the brightest emission remains centered on the putative pulsar position.

2.2. Spectral analysis

Spectral information was obtained between 0.2 and 30 TeV in two distinct regions corresponding to the best morphological model. The central and annular emissions were analyzed within a circular region of 0.1° radius and between $r_{\rm min}$ = 0.1° and $r_{\rm max}$ = 0.3° respectively. The *reflected region background* technique (Berge et al. 2007) was used to evaluate the background in the FoV. The spectrum of the central region is well fitted by a pure power law (equivalent χ^2/ndf = 22/18) defined as:

$$\frac{{\rm d}N}{{\rm d}E} = \Phi(E_{\rm dec}) \times \left(\frac{E}{E_{\rm dec}}\right)^{-\Gamma}, \quad (1)$$

where the decorrelation energy $E_{\rm dec}$ is the energy at which the correlation between the flux normalization (Φ) and spectral index Γ is zero and where the statistical errors are the smallest. The best-fit parameters, listed in Table 2, yield an integrated flux $I_{1-30\ \rm TeV} = (0.40 \pm 0.05_{\rm stat} \pm 0.08_{\rm syst}) \times 10^{-12}$ cm^{-2} s^{-1}, which corresponds to ∼2% of the Crab nebula flux in the same energy range. The use of an exponential cutoff power-law model improves the fit at a 2.4σ level, slightly lower than the improvement level reported in Méhault et al. (2011), but still in agreement with it. In the following, the pure power-law shape is considered.

The spectrum extracted from the annular region follows a power-law shape (χ^2/ndf = 37/32) with the best-fit parameters reported in Table 2. The integrated flux $I_{1-30\ \rm TeV} = (1.13 \pm 0.11_{\rm stat} \pm 0.23_{\rm syst}) \times 10^{-12}$ cm^{-2} s^{-1} corresponds to ∼5% of the Crab nebula. No significant difference between the spectral indices in the central and annular regions was detected. The sum of the integral fluxes calculated in each region agrees with the flux found in the total emission, which is well fitted by a power-law model (parameters listed in Table 2). Figure 5 shows the H.E.S.S. spectral points for the annular and central regions and 1σ statistical errors. The bowties represent the 1σ error contours of the spectra. The measured fluxes and spectral indices for these regions given in Table 2 and Fig. 5 are reliable, because these regions are larger than the H.E.S.S. PSF, and the H.E.S.S. PSF shows little variation with energy.

As explained in Sect. 2.1, the VHE γ-ray emission was modeled by the sum of two components: one point-like and one extended. To estimate the intrinsic flux of each component and to model the spectral energy distribution (SED), the spectral points

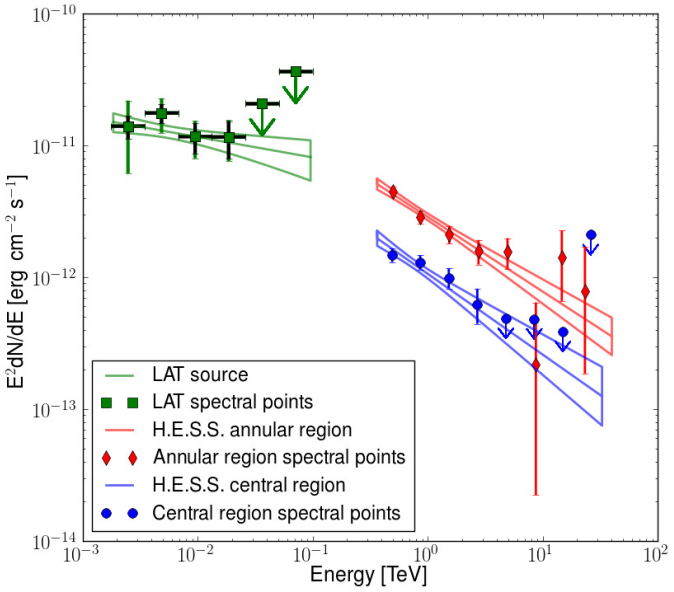

Fig. 5. Spectral points and bowties of the LAT source (squares - statistical and systematic uncertainties added in quadrature in green and only statistical errors in black) and the H.E.S.S. annular (red diamonds) and central (blue points) regions. Bowties represent the 1σ confidence level error on spectra. The upper limits are calculated for a 3σ confidence level.

extracted in the central and annular regions (see Fig. 5) were corrected for the contributions of each component in each region. To normalize only their flux, a constant spectral index at any distance from the putative pulsar was assumed, in agreement with the spectral fits (see Table 2). From the best morphological model, the contributions of the point-like and extended components to the total flux were calculated to be 64% ± 4% and 36% ± 4% of the central region flux ($r < 0.1°$), respectively. The point-like component contribution to the total flux emission in the annular region is 17% ± 2%.

3. *Fermi* LAT observations and analysis

The following analysis was performed using 47 months of data acquired from 2008 August 4 to 2012 June 30 within a 15° × 15° square around the position of the SNR W41. Only γ-ray events with reconstructed zenith angles smaller than 100° were selected to reduce contamination from γ rays from cosmic-ray interactions in the upper atmosphere. In addition, time intervals were excluded when the rocking angle was wider than 52° and when the *Fermi* satellite was in the South Atlantic Anomaly. Events were selected from 1.8 GeV to 100 GeV in the Pass 7 Source class (Ackermann et al. 2012). The *P7_SOURCE_V6* instrument response functions (IRFs) were used. This selection is motivated by the morphological stability of the source, the improved angular resolution at high energy, and the difficulties in modeling the Galactic diffuse emission, that implies large systematic errors at low energy. These effects can be seen in the low-energy part ($E < 1$ GeV) of the spectrum in Castro et al. (2013). Two different tools using the maximum-likelihood technique (Mattox et al. 1996) were applied to perform the spatial and spectral analysis: `pointlike` (Lande et al. 2012) and *Fermi* LAT Science Tools[1]. These tools fit a source model to the data along with models for the residual charged particles, diffuse γ-ray emission, and the LAT sources in the region of interest listed in the second LAT catalog (Nolan et al. 2012). To describe the Galactic diffuse emission, the ring-hybrid model *gal_2yearp7v6_v0.fits* was used. The instrumental background and the extragalactic radiation are described by a single isotropic component with the spectral shape in the tabulated model *iso_p7v6source.txt*. These models are available from the *Fermi* Science Support Center[2].

All 2FGL sources within 20° radius around W41 were added to the spectral-spatial model of the region. Lande et al. (2012) studied the region surrounding HESS J1837−069 ($l \sim 25.3°; b \sim -0.3°$) in detail based on the LAT catalog. The best-fit model (including spectrum) for this region was used. The source 2FGL J1837.3−0700c was modeled with a symmetrical Gaussian ($\sigma \simeq 0.33°$). The two closest sources, 2FGL J1834.7−0705c and 2FGL J1836.8−0623c, were relocalized although their positions did not significantly change.

3.1. Search for pulsed emission

The *Fermi* LAT is the first instrument sensitive enough to discover new pulsars based on their γ-ray pulsations alone (Abdo et al. 2009a): 41 new γ-ray pulsars have been detected to date in this way. To check for the presence of a γ-ray pulsar in W41, a search for pulsations in *Fermi* LAT data using the hierarchical blind-search technique described in Pletsch et al. (2012) was performed. To improve the signal-to-noise ratio (S/N) of the putative pulsar in W41, each photon was assigned a probability that it originates from the target source, using the spectral model obtained from the analysis described in Sect. 3.3. While the faintest pulsars detected in blind searches have $S/N \sim 15$, in the case of W41, $S/N \leq 1$: no significant pulsations were found.

3.2. Morphological analysis

Figure 6 shows the test statistic (TS) map between 1.8 and 100 GeV, with H.E.S.S. significance contours (from 3 to 8σ) overlaid. The TS is defined as twice the difference between the log-likelihood L_1 obtained by fitting a source model plus the background model to the data, and the log-likelihood L_0 obtained by fitting the background model alone, that is, $\mathrm{TS} = 2\ln(L_1 - L_0)$. This skymap contains the TS value for a point source at each map location, thus giving a measure of the statistical significance for the detection of a γ-ray source in excess of the background. The source is detected with $\mathrm{TS}_{\mathrm{max}} = 111$ above 1.8 GeV. During the fit, the spectral parameters of sources closer than 5° to W41 were allowed to vary in the likelihood fit as well as the normalization of the diffuse models, while the parameters of all other sources were fixed at the values of the 2FGL catalog. The source extension was determined using `pointlike` with a Gaussian hypothesis (compared with a point-source hypothesis). The difference in TS between the Gaussian and the point-source hypothesis is 20, which converts to a significance of $\sim 4.5\sigma$. This suggests that the source is extended with respect to the LAT PSF. The intrinsic size is $\sigma_{\mathrm{GeV}} = (0.15° \pm 0.03°)$ and the best-fit position ($l = 23.20° \pm 0.03°$, $b = -0.28° \pm 0.03°$) is compatible with the candidate pulsar position. This morphology is shown in Fig. 4. An asymmetric Gaussian distribution was also considered but did not improve the fit with respect to the Gaussian hypothesis ($\Delta\mathrm{TS} = 1.5$).

[1] http://fermi.gsfc.nasa.gov/ssc/

[2] http://fermi.gsfc.nasa.gov/ssc/data/access/lat/BackgroundModels.html

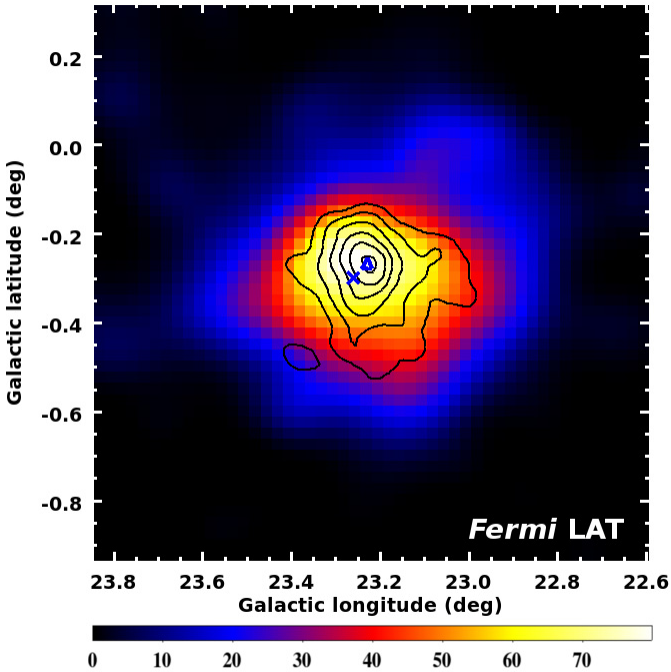

Fig. 6. *Fermi* LAT TS map of the W41 region, above 1.8 GeV. The TS was evaluated by placing a point-source at the center of each pixel, Galactic diffuse emission and nearby 2FGL sources are included in the background model. H.E.S.S. significance contours (3, 4, 5, 6, 7 and 8σ) are overlaid as black solid lines. The triangle and the cross indicate the position of the putative pulsar and the OH maser.

3.3. Spectral analysis

The spectrum of the *Fermi* LAT source was estimated with `gtlike` taking into account the sky model and the shape obtained with `pointlike`. The spectrum is well described by a power law (see Eq. (1)). The best-fit parameters are $\Phi(E_{\rm dec}) = (4.98 \pm 0.20_{\rm stat} \pm 0.22_{\rm syst}) \times 10^{-13}$ cm^{-2} s^{-1} MeV^{-1}, $E_{\rm dec} = 4088$ MeV, and $\Gamma = 2.15 \pm 0.12_{\rm stat} \pm 0.16_{\rm syst}$. These results are compatible with the parameters found by Castro et al. (2013).

Two main sources of systematic errors were considered: imperfect modeling of the Galactic diffuse emission and uncertainties in the effective area. The first one was estimated by artificially changing the normalization of the Galactic diffuse model by ±6%, as in Abdo et al. (2010e). The second one was estimated by using modified IRFs whose effective areas bracket the nominal IRFs. These bracketing IRFs are defined by envelopes above and below the nominal energy dependence of the effective area by linearly connecting differences of (10%, 5%, 20%) at log(E/MeV) of (2, 2.75, 4), respectively (Ackermann et al. 2012).

The *Fermi* LAT spectral points were obtained by dividing the energy range (1.8−100 GeV) into six logarithmically spaced energy bins. A Bayesian upper limit (Loparco et al. 2011) at a 3σ confidence level was calculated if the TS value in the energy bin was lower than 9. The LAT spectral points and their uncertainties are reported in Fig. 5.

The scenario where the emission seen with *Fermi* LAT is produced by two components was investigated by fixing the best-fit extension and position found in GeV and adding a point-like source at the putative pulsar position. In this case, the point-like source is not significant (TS $\simeq$ 7) and a Bayesian upper limit on its integrated flux was calculated: $S(1.8{-}100\ {\rm GeV}) < 1.0 \times 10^{-12}$ erg cm^{-2} s^{-1} at a 3σ confidence level.

4. Discussion

Follow-up observations of the previously discovered source HESS J1834−087 as described here have led to the discovery of a two-component morphology: a central point-like and an extended component. *Fermi* LAT observations were also analyzed in the GeV energy band, leading to the detection of a γ-ray source (2FGL J1834.3−0848) coincident with the TeV source and with a similar extension. Figure 4 highlights that the positions of both the TeV and GeV sources are compatible with each other and also with SNR W41. This new information is very useful to constrain the nature of the γ-ray source.

In addition to the extended emission, no significant point-like component was detected using *Fermi* LAT data, in contrast with H.E.S.S. (see Sect. 2.1). With *Fermi* LAT observations, Abdo et al. (2013) have found that pulsar spectra usually follow a power law with an exponential cutoff at energies between 1 and 10 GeV. However, such a cutoff is not apparent in the spectrum derived in Sect. 3.3. Moreover, no γ-ray pulsations from the putative pulsar at the center of the remnant were detected. These arguments and the fact that the γ-ray emission observed with *Fermi* LAT is significantly extended strongly suggest that the signal does not arise from an unseen pulsar.

It is clear from Fig. 1 that the VHE γ-ray emission does not correlate with the SNR radio shell, but comes from the center of the remnant, as shown by the VHE radial profile in Fig. 2. This disfavors a scenario in which the signal originates in the SNR shell, in contrast with the case of RX J1713.7−3946 (Aharonian et al. 2004) for example.

Therefore, only two plausible scenarios remain: either the γ-ray emission is produced by a PWN powered by the pulsar candidate CXOU J183434.9−084443 detected in X-rays, or it is caused by the interaction of the SNR with a nearby MC.

Unless otherwise specified, an assumed distance of $d = 4.2$ kpc was considered in the following sections.

4.1. Pulsar wind nebula candidate scenario

The increasing number of detected PWNe at VHE motivated us to investigate a scenario where the GeV and TeV γ-ray emission is produced by the wind of the putative pulsar CXOU J183434.9−084443.

4.1.1. TeV source HESS J1834−087 as a single source powered by the putative pulsar

The spatial coincidence between the centroid of the GeV and the TeV emissions and the pulsar candidate strengthens this hypothesis, as also stated by Misanovic et al. (2011). Interestingly, assuming that the extended component detected in X-rays is a PWN, Misanovic et al. (2011) found that the ratio of the extended source and pulsar candidate X-ray luminosities, $L_{\rm PWN_X}/L_{\rm PSR_X} \sim 1.8$, is typical of a PWN/pulsar system. Furthermore, the PWN scenario is reasonable from an energetic point of view. Indeed, assuming a distance of $d = 4.2$ kpc, Misanovic et al. (2011) derived an X-ray luminosity of $L_{\rm X}(2{-}10\ {\rm keV}) \simeq 1 \times 10^{33}$ erg s^{-1}. Then, assuming a termination shock radius $r_{\rm s,17} = r_{\rm s}/(10^{17}\ {\rm cm})$ scaled to a plausible value (corresponding to an angular size of 2.7″ at the assumed distance) and an ambient pressure $p_{\rm amb,-9} = p_{\rm amb}/(10^{-9}$ dyne cm$^{-2})$ inside the SNR in the Sedov expansion phase, the authors derived a spin-down luminosity of $\dot{E} = 4 \times 10^{36} \times r_{\rm s,17}^2 \times p_{\rm amb,-9}$ erg s^{-1}, which is typical for Vela-like pulsars and supports the assumption of a young PWN. This value is consistent with the estimates

Table 3. Fitted parameters of the SED modeling shown in Fig. 7 assuming HESS J1834−087 is a single physical source as observed from the GeV to the TeV range.

Fit parameters	Leptonic model and Maxwellian temperature at 66.9 ± 0.3 GeV	Hadronic model from Li & Chen (2012)
τ (kyr)	10	100
B (μG)	14.1 ± 0.8	10
W_e or W_p ($\times 10^{49}$ erg)[a]	0.24 ± 0.05	10.0
Γ_{inj}	−2.6 ± 0.3	−2.2
$E_{c,e}$ or $E_{c,p}$ (TeV)	13.4 ± 3.9	50

Notes. The leptonic model consists of a low-energy Maxwellian distribution for the electrons. The hadronic model parameters are those found by Li & Chen (2012). The spectra of electrons e and protons p are represented by a power law of slope Γ_{inj} with an exponential cutoff at energy $E_{c,e}$ and $E_{c,p}$, respectively. [(a)] Total energy in electrons or protons (depending on the model).

of $[10^{36}, 10^{37}]$ erg s^{-1} that can be derived from Kargaltsev & Pavlov (2008). Pulsars associated with several TeV PWNe have a similar spin-down power (Gallant et al. 2008).

From the data analyses described in the previous sections, the GeV and TeV luminosities are estimated to be $L_{GeV}(1-100\ \mathrm{GeV}) \simeq 1.6 \times 10^{35}$ erg s^{-1} and $L_{TeV}(1-30\ \mathrm{TeV}) \simeq 1.1 \times 10^{34}$ erg s^{-1}, the latter being calculated for the entire emitting region. Mattana et al. (2009) used a large sample of PWNe observed in X-rays and γ-rays to demonstrate the correlation between the luminosity ratio L_{TeV}/L_X and the characteristic age τ_c of the powering pulsar. Using the luminosities derived from *XMM-Newton* and H.E.S.S. observations, the characteristic age is in the range $\tau_c \in [3 \times 10^3, 6 \times 10^4]$ yr, which is younger than the estimated age of the remnant (tentative remnant dating: $t_{SNR} \in [6 \times 10^4, 2 \times 10^5]$ yr ; see Sect. 1).

At the assumed distance of 4.2 kpc, the radius of the nebula in the TeV range is $r \simeq 12$ pc. A corresponding age of $[6 \times 10^3, 2 \times 10^4]$ yr is obtained by modeling the PWN evolution inside the SNR (Reynolds & Chevalier 1984) with a mass of the progenitor $M \sim 8\ M_\odot$, an explosion energy $E_0 \sim 10^{51}$ erg, a spin-down luminosity of $\dot{E} \in [10^{36}, 10^{37}]$ erg s^{-1}, and a density inside the shell $n = 0.1$ cm^{-3}. By using standard values, this age agrees with the estimated characteristic age of the putative pulsar described above, but is still younger than the interval proposed for the remnant.

Therefore, if HESS J1834−087 is a PWN powered by the putative pulsar CXOU J183434.9−084443, this would imply that the SNR W41 might be younger than 6×10^4 yr, or that W41 is located at a distance smaller than the assumed value, or that the pulsar and the TeV source are simply not related to W41. These conclusions are strongly dependent on the input parameters and were derived assuming an evolutionary phase before the crushing by the reverse shock supported by the X-ray observations described above. Therefore, they must be considered as indicators only.

An SED modeling has been performed assuming that the whole TeV source is associated with the GeV emission. However, unlike most PWNe detected by *Fermi* LAT, which present a hard spectrum with an average spectral index $\Gamma \sim 1.8$ (Acero et al. 2013), the *Fermi* LAT spectrum of HESS J1834−087 is rather soft. In this sense, this γ-ray source resembles HESS J1640−465, for which Slane et al. (2010) inferred a distinct population of low-energy electrons based on the particle-in-cell simulations performed by Spitkovsky (2008). We used a similar reasoning by modeling the low-energy part of the electron spectrum by an additional Maxwellian distribution. The solid black curve in Fig. 7 represents the obtained fitted leptonic model ($\chi^2/ndf = 10.5/7$). The output parameters are listed in Table 3 and are discussed below. The cosmic microwave

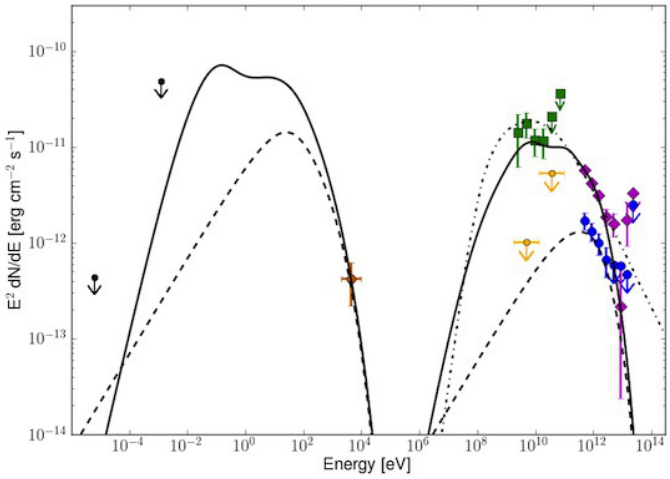

Fig. 7. Spectral energy distribution (SED) for three different assumptions about the nature of the source. Solid line: The association between a single TeV source (violet diamonds) and the GeV source (green squares) has been assumed. A leptonic scenario has been tested where a low-energy Maxwellian distribution replaces the low-energy part of the electron spectrum. The fitted parameters of this model can be found in Table 3. Dashed line: a simple leptonic model has been tested assuming the TeV point-like source (blue points) is associated with a hypothetical GeV point-like source superimposed on the extended one (yellow upper limits). The blue TeV spectral points have been obtained after normalizing the points computed in the central extracted region (see Sect. 2.2 for details). Dash-dotted line: the hadronic model studied by Li & Chen (2012) has been superimposed to the new data points obtained in this work. The brown X-ray spectral point has been derived from the *XMM-Newton* spectrum given by Mukherjee et al. (2009), the black radio upper limits from VLA 20 cm (Helfand et al. 2006) and Bolocam 1.1 mm (Aguirre et al. 2011) images.

background and the Galactic interstellar radiation field at the location of the SNR W41, used to calculate the inverse Compton emission, were derived from the estimates of Porter & Strong (2005). The energy densities for the IR and optical photon fields are 1.6 eV cm^{-3} and 2.2 eV cm^{-3}, respectively. The characteristic age of the pulsar was assumed to be $t = 10$ kyr, close to the mean of the ranges previously estimated. The best-fit magnetic field value ($B \simeq 14\ \mu$G) is similar to the values found for other TeV PWNe (de Jager & Djannati-Ataï 2009). The derived total energy in electrons is $W_e \simeq 2.4 \times 10^{48}$ erg. Assuming a constant spin-down power over the entire lifetime of the pulsar, this energy corresponds to ∼700% or ∼70% of the total energy injected by the pulsar for a spin-down power of 10^{36} erg s^{-1} or 10^{37} erg s^{-1}, respectively. In this context, if the whole GeV and TeV emissions correspond to the same PWN, the spin-down

power of the pulsar must be close to (or even higher than) $\sim 10^{37}$ erg s^{-1} at present, assuming a constant energy-loss rate, or was much higher than 10^{36} erg s^{-1} in the past and decreased with time. A precise modeling of the evolution of the spin-down power and magnetic field with time is beyond the scope of this paper, since most parameters for such a model are poorly constrained.

4.1.2. Only the TeV point-like component is powered by the putative pulsar

In an alternative PWN scenario, we assumed that only the TeV point-like component (spatially coincident with the X-ray point-like source) is produced by the PWN powered by the putative pulsar. Under this assumption, the γ-ray efficiency is estimated to be $L_{\rm TeV}/\dot{E} \in [0.1\%, 1\%]$. This is consistent with the range of efficiencies (0.01–10%) found for several VHE PWNe candidates (Gallant et al. 2008).

A simple one-zone leptonic model was considered and is displayed in Fig. 7 (dashed line). The TeV data were computed from the normalized data found in the central extraction region that are displayed in Fig. 5. The calculation of the normalization is detailed in Sect. 2.2. Despite the large spectral uncertainties, an SED modeling was performed to estimate the physical parameters of the source. The model assumes a distribution of accelerated electrons that cool radiatively by means of synchrotron radiation and inverse-Compton scattering, a distance of 4.2 kpc, and an age of 10^4 yr for the pulsar. This age is younger than that estimated for W41, but still in the estimated range for τ_c. A good representation of the radio upper limits and X-ray data together with the GeV point-like source upper limits and TeV central component is obtained for an injection spectral index $\Gamma_{\rm inj} = -2.0$ and a magnetic field of $B \simeq 15\ \mu$G. The total energy injected to leptons ($W_e \simeq 3.0 \times 10^{47}$ erg) represents ~10% (or 100%) of the rotational energy that can be injected by the pulsar over its entire lifetime, assuming a constant rotational power of 10^{37} erg s^{-1} (or 10^{36} erg s^{-1}, respectively), which again favors a spin-down power higher than 10^{36} erg s^{-1} for the powering pulsar.

In this scenario, the TeV point-like source is assumed to be unrelated to the TeV extended component. Thus, the extended structure seen by *Fermi* LAT and H.E.S.S. may have two possible origins. Electrons accelerated in the past and affected by radiative losses could create a relic nebula that emits in γ-rays. This ancient PWN would be too faint to be detected in X-rays. An energy-dependent morphology of the γ-ray emission from 1.8 GeV up to 100 TeV might suggest electron cooling in the PWN. However, without any significant variation of the intrinsic sizes of the γ-ray source in this energy range or variation of the spectral slope at VHE energy, this scenario tends to be disfavored. The other possibility suggests that the emission from the interaction of the SNR with the MC is in the line of sight of the PWN γ-ray emission. But the chance probability of detecting two TeV sources in spatial coincidence in the part of the Galactic plane covered by H.E.S.S. (140° × 6°) was estimated to be $p \simeq 9.4 \times 10^{-4}$ from the formula in Akujor (1987). Nevertheless, this configuration may occur, as in the case of W51C, where the TeV source seems to be powered by a PWN and an SNR/MC interaction (Aleksić et al. 2012; Feinstein et al. 2009).

4.2. SNR-MC interaction

Using high-resolution CO observations, Tian et al. (2007) suggested that a MC is located close to the SNR W41 and could even be interacting with the SNR, as proposed by Albert et al. (2006). The γ-ray emission detected by H.E.S.S. (as seen in Fig. 1) is spatially coincident with the ^{13}CO high-density region extracted from GRS data (Jackson et al. 2006), as observed for other interacting SNRs at TeV energy. Direct evidence that the shock wave of W41 is interacting with a MC has been discovered recently. Frail et al. (2013) found two regions with OH maser emission close to the center of the remnant. Only the brightest maser at $l, b = (23.26°, -0.31°)$ is displayed in Figs. 1, 4, and 6.

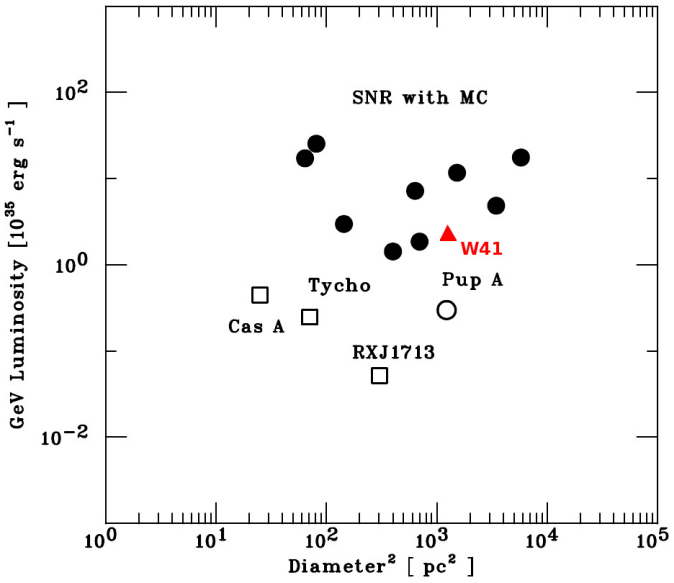

Fig. 8. GeV luminosity (0.1−100 GeV) as a function of diameter squared for each of the SNRs detected with *Fermi* LAT (Thompson et al. 2012). Filled circles correspond to the SNRs interacting with molecular clouds. Rectangles represent young SNRs. Puppis A, a middle-aged SNR without clear molecular interaction, is shown as an open circle. The source coincident with the SNR W41 is marked by a red triangle.

Fermi LAT observations have already led to the detection of γ-ray emission from several SNRs. Interestingly, SNRs interacting with MCs constitute the dominant class of γ-ray luminous SNRs, and several evolved interacting remnants (i.e., W51C, W44, IC443, and W28) are associated with extended GeV emission (Abdo et al. 2009b, 2010b,c,d). For W41, the estimated luminosity L(0.1−100 GeV) assuming $d = 4.2$ kpc is similar to that of other interacting SNRs detected by *Fermi*, as shown in Fig. 8 (Thompson et al. 2012). In this context, Li & Chen (2012) proposed an accumulated diffusion model in which the MC size is taken into account and where the diffusion distance of the injected protons varies as the remnant expands. This illuminated cloud model reproduces the GeV and TeV emission using a reasonable energy budget: the total energy injected up to $E_{\rm max} \simeq 50$ TeV is $W_p \simeq 10^{50}$ erg. The set of parameters is summarized in Table 3 and reproduced in Fig. 7 (dash-dotted line). This model was obtained from the spectrum published in Méhault et al. (2011). The flat spectrum seen by *Fermi* up to several tens of GeV implies a break at ~100 GeV, which is unusual for interacting SNRs. This led Li & Chen (2012) to use a cloud as large as the shock wave radius and a diffusion coefficient lower than the average Galactic value. This may occur if the interstellar medium is highly ionized by cosmic rays.

5. Conclusion

Follow-up observations have been performed from 1.8 GeV to up to 100 TeV in the direction of the SNR W41 to provide new

clues on the origin of the γ-ray emission. In the VHE domain, the H.E.S.S. data exhibit a two-component morphology: a central point-like source and an extended component. The detailed study of *Fermi* LAT HE γ-ray observations revealed extended emission with an intrinsic size (0.15°) similar to that of the TeV extended component (0.17°). The GeV and TeV emissions are spatially coincident with a candidate pulsar located at the center of the remnant. However, no pulsations in radio, X-rays, or HE γ-rays were detected. Different scenarios were investigated to explain the γ-ray emission.

First, the spatial coincidence of the best-fit position of the γ-ray sources with an X-ray CCO possibly surrounded by a PWN strengthens the PWN scenario. The potential CCO is able to power the whole γ-ray emission only if its current spin-down is close to (or even higher than) 10^{37} erg s^{-1}. Then, the flat GeV spectrum can only be reproduced assuming a second low-energy electron population. These two aspects are very similar to the case of the PWN candidate HESS J1640-465 (Slane et al. 2010).

Second, the extended GeV and the whole TeV sources are coincident with a high-density region traced by ^{13}CO. A model based on the assumption of an interaction between W41 and the nearby MC reproduces the spectral data with a reasonable energy budget. Because of the flat *Fermi* LAT spectrum, an unusually high-energy spectral break at ~100 GeV is required. However, the interacting scenario is reinforced by the recent discovery of OH (1720 MHz) maser lines coincident with the remnant and compatible with the associated cloud velocity.

The last possibility would be that the TeV emission has two different sources. The point-like component would originate from the PWN powered by the putative pulsar, while the extended TeV component that matches the GeV source would be created by the interaction between the remnant and the cloud. In this case, the spatial coincidence between the point-like and the extended VHE γ-ray emission would occur by chance, but the probability is very low.

Nevertheless, the hadronic scenario seems to explain both GeV and TeV extended emission, as argued in this work. This origin is supported by the recent maser detection and theoretical studies of this γ-ray source.

A clear identification of the extended component in X-rays could help to investigate the hypothesis of a PWN, but given the low-energy flux expected from typical relic PWNe, this appears to be a serious observational challenge. Deeper VHE observations with the Cherenkov Telescope Array (CTA) might also allow higher energy resolution studies and a firm identification of the origin of the VHE emission, in particular through morphological analysis. Concerning the *Fermi* LAT analysis, the next improvement of the Galactic diffuse emission model and the IRFs might ameliorate the study of the GeV γ-ray emission at lower energies in order to better constrain the modeling of the spectral energy distribution.

Acknowledgements. The support of the Namibian authorities and of the University of Namibia in facilitating the construction and operation of H.E.S.S. is gratefully acknowledged, as is the support by the German Ministry for Education and Research (BMBF), the Max Planck Society, the French Ministry for Research, the CNRS-IN2P3 and the Astroparticle Interdisciplinary Programme of the CNRS, the UK Science and Technology Facilities Council (STFC), the IPNP of the Charles University, the Polish Ministry of Science and Higher Education, the South African Department of Science and Technology and National Research Foundation, and by the University of Namibia. We appreciate the excellent work of the technical support staff in Berlin, Durham, Hamburg, Heidelberg, Palaiseau, Paris, Saclay, and in Namibia in the construction and operation of the equipment. The *Fermi* LAT Collaboration acknowledges generous ongoing support from a number of agencies and institutes that have supported both the development and the operation of the LAT as well as scientific data analysis. These include the National Aeronautics and Space Administration and the Department of Energy in the United States, the Commissariat à l'Énergie Atomique and the Centre National de la Recherche Scientifique/Institut National de Physique Nucléaire et de Physique des Particules in France, the Agenzia Spaziale Italiana and the Istituto Nazionale di Fisica Nucleare in Italy, the Ministry of Education, Culture, Sports, Science and Technology (MEXT), High Energy Accelerator Research Organization (KEK) and Japan Aerospace Exploration Agency (JAXA) in Japan, and the K. A. Wallenberg Foundation, the Swedish Research Council and the Swedish National Space Board in Sweden. Additional support for science analysis during the operations phase is gratefully acknowledged from the Istituto Nazionale di Astrofisica in Italy and the Centre National d'Études Spatiales in France.

References

Abdo, A. A., Ackermann, M., Ajello, M., et al. (Fermi Collaboration) 2009a, Science, 325, 840
Abdo, A. A., Ackermann, M., Ajello, M., et al. (Fermi Collaboration) 2009b, ApJ, 706, L1
Abdo, A. A., Ackermann, M., Ajello, M., et al. (Fermi Collaboration) 2010a, ApJS, 188, 405
Abdo, A. A., Ackermann, M., Ajello, M., et al. (Fermi Collaboration) 2010b, Science, 327, 1103
Abdo, A. A., Ackermann, M., Ajello, M., et al. (Fermi Collaboration) 2010c, ApJ, 712, 459
Abdo, A. A., Ackermann, M., Ajello, M., et al. (Fermi Collaboration) 2010d, ApJ, 718, 348
Abdo, A. A., Ackermann, M., Ajello, M., et al. (Fermi Collaboration) 2010e, ApJ, 722, 1303
Abdo, A. A., Ajello, M., Allafort, A., et al. (Fermi Collaboration) 2013, ApJS, 208, 17
Abramowski, A., Acero, F., Aharonian, F., et al. (H.E.S.S. Collaboration) 2011, A&A, 533, A103
Acero, F., Ackermann, M., Ajello, M., et al. (Fermi Collaboration) 2013, ApJ, 773, 77
Ackermann, M., Ajello, M., Albert, A., et al. (Fermi Collaboration) 2012, ApJS, 203, 4
Aguirre, J. E., Ginsburg, A. G., Dunham, M. K., et al. 2011, ApJS, 192, 4
Aharonian, F., & Atoyan, A. M. 1996, A&A, 309, 917
Aharonian, F., Akhperjanian, A. G., Aye, K.-M., et al. (H.E.S.S. Collaboration) 2004, Nature, 432, 75
Aharonian, F., Akhperjanian, A. G., Aye, K.-M., et al. (H.E.S.S. Collaboration) 2005a, Science, 307, 1938
Aharonian, F., Akhperjanian, A. G., Aye, K.-M., et al. (H.E.S.S. Collaboration) 2005b, Science, 309, 746
Aharonian, F., Akhperjanian, A. G., A. R. Bazer-Bachi, et al. (H.E.S.S. Collaboration) 2006a, A&A, 457, 899
Aharonian, F., Akhperjanian, A. G., Bazer-Bachi, A. R., et al. (H.E.S.S. Collaboration) 2006b, A&A, 636, 777
Aharonian, F., Akhperjanian, A. G., Bazer-Bachi, A. R., et al. (H.E.S.S. Collaboration), 2006c, A&A, 460, 743
Aharonian, F., Akhperjanian, A. G., Bazer-Bachi, A. R., et al. (H.E.S.S. Collaboration), 2006d, A&A, 448, L43
Akujor, C. E. 1987, Ap&SS, 135, 187
Albert, J., Aliu, E., Anderhub, H., et al. (MAGIC Collaboration) 2006, ApJ, 643, L53
Aleksić, J., Alvarez, E. A., Antonelli, L. A., et al. (MAGIC Collaboration) 2012, A&A, 541, 13
Atwood, W. B., Abdo, A. A., Ackermann, M., et al. (Fermi Collaboration) 2009, ApJ, 697, 1071
Berge, D., Funk, S., Hinton J., et al. 2007, A&A, 466, 1219
Carrigan, S., Brun, F., Chaves, R. C. G., et al. 2013, ICRC, in press [arXiv:1307.4690]
Castro, D., Slane, P., Carlton, A., et al. 2013, ApJ, 774, 36
Cox, D., 1972, ApJ, 178, 159
de Jager, O. C., & Djannati-Ataï, A. 2009, ASSL, 357, 451
Fazio, G. G., Hora, J. L., Allen, L. E., et al. 2004, ApJS, 154, 10
Feinstein, F., Fiasson, A., Gallant, Y., et al. 2009, AIP Conf. Proc., 1112, 54
Frail, D. A., Claussen, M. J., Méhault J. 2013, ApJ, 773, L19
Gaensler, B. M., & Johnson, S. 1995, MNRAS, 275, L73
Gallant, Y. A., Carrigan, S., Djannati Ataï, A., et al. 2008, AIP Conf. Proc., 983, 195
Grondin, M. H., Funk, S., Lemoine-Goumard, M., et al. 2011, ApJ, 738, 42
Helfand, D. J., Becker, R. H., White, R. L., et al. 2006, AJ, 131, 2525
Jackson, J. M., Rathborne, J. M., & Shah, R. Y. 2006, ApJS, 163, 145
Kargaltsev, O., & Pavlov, G. G., 2008, in 40 Years of Pulsars: Millisecond Pulsars, Magnetars and More, eds. C. Bassa, Z. Wang, A. Cumming, & V. M. Kaspi (Melville, NY: AIP), AIP Conf. Ser., 983, 171
Kennel, C. F., & Coroniti, F. V. 1984, ApJ, 283, 694

Lande, J., Ackermann, M., Allafort, A., et al. 2012, ApJ, 756, 5
Leahy, D. A., & Tian, W. W. 2008, AJ, 135, 167
Li, H., & Chen, Y. 2012, MNRAS, 421, 935
Lockett, P., Gauthier, E., Elitzur, M., et al. 1999, ApJ, 511, 235
Loparco, F., & Mazziotta, M. N. 2011, Nucl. Instrum. Meth., 646, 167
Mattana, F., Falanga, M., Götz, D., et al. 2009, ApJ, 694, 12
Mattox, J. R., Bertsch, D. L., Chiang, J., et al. 1996, ApJ, 461, 396
Méhault, J., Cohen-Tanugi, J., Grondin, M.-H., et al. 2011, ICRC, 7, 180
Misanovic, Z., Kargaltsev, O., Pavlov, G. G., et al. 2011, ApJ, 735, 33
Mukherjee, R., Gotthelf, E. V., Halpern, J. P., et al. 2009, ApJ, 691, 1707
de Naurois, M., & Rolland, L. 2009, Astropart. Phys., 32, 231
Nolan, P. L., Abdo, A. A., Ackermann, M., et al. (Fermi Collaboration) 2012, ApJS, 199, 31
Pletsch, H. J., Guillemot, L., Allen, B., et al. 2012, ApJ, 744, 105
Porter, T. A., & Strong, A. W. 2005, ICRC, 4, 77
Reynolds, S. P., & Chevalier, R. A. 1984, ApJ, 278, 630
Rieke, G. H., Young, E.T., Engelbracht, C.W., et al. 2004, ApJS, 154, 25
Slane, P., Castro, D., Funk, S., et al. 2010, ApJ, 720, 266
Smith, D. A., Guillemot, L., Camilo, F., et al. 2008, A&A, 492, 923S
Spitkovsky, A. 2008, ApJ, 682, L5
Thompson, D. J., Baldini, L., Uchiyama, Y., 2012, APh, 39, 22
Tian, W. W., Li, Z., Leahy, D. A., Wang, Q. D., et al. 2007, ApJ, 657, L25
Uchiyama, Y., Blandford, R. D., Funk, S., et al. 2010, ApJ, 723, L122
White, R. L., Becker, R. H., & Helfand, D. J. 2005, AJ, 130, 586

[1] Universität Hamburg, Institut für Experimentalphysik, Luruper Chaussee 149, 22761 Hamburg, Germany
[2] Max-Planck-Institut für Kernphysik, PO Box 103980, 69029 Heidelberg, Germany
[3] Dublin Institute for Advanced Studies, 31 Fitzwilliam Place, Dublin 2, Ireland
[4] National Academy of Sciences of the Republic of Armenia, 375014 Yerevan, Armenia
[5] Yerevan Physics Institute, 2 Alikhanian Brothers St., 375036 Yerevan, Armenia
[6] Institut für Physik, Humboldt-Universität zu Berlin, Newtonstr. 15, 12489 Berlin, Germany
[7] Universität Erlangen-Nürnberg, Physikalisches Institut, Erwin-Rommel-Str. 1, 91058 Erlangen, Germany
[8] University of Namibia, Department of Physics, 13301 Private Bag, Windhoek, Namibia
[9] University of Durham, Department of Physics, South Road, Durham DH1 3LE, UK
[10] DESY, 15738 Zeuthen, Germany
[11] Institut für Physik und Astronomie, Universität Potsdam, Karl-Liebknecht-Strasse 24/25, 14476 Potsdam, Germany
[12] Nicolaus Copernicus Astronomical Center, ul. Bartycka 18, 00-716 Warsaw, Poland
[13] Department of Physics and Electrical Engineering, Linnaeus University, 351 95 Växjö, Sweden
[14] Institut für Theoretische Physik, Lehrstuhl IV: Weltraum und Astrophysik, Ruhr-Universität Bochum, 44780 Bochum, Germany
[15] Institut für Astro- und Teilchenphysik, Leopold-Franzens-Universität Innsbruck, 6020 Innsbruck, Austria
[16] Laboratoire Leprince-Ringuet, École Polytechnique, CNRS/IN2P3, 91128 Palaiseau, France
[17] now at Santa Cruz Institute for Particle Physics, Department of Physics, University of California at Santa Cruz, Santa Cruz CA 95064, USA
[18] Centre for Space Research, North-West University, 2520 Potchefstroom, South Africa
[19] LUTH, Observatoire de Paris, CNRS, Université Paris Diderot, 5 Place Jules Janssen, 92190 Meudon, France
[20] LPNHE, Université Pierre et Marie Curie Paris 6, Université Denis Diderot Paris 7, CNRS/IN2P3, 4 Place Jussieu, 75252 Paris Cedex 5, France
[21] Institut für Astronomie und Astrophysik, Universität Tübingen, Sand 1, 72076 Tübingen, Germany
[22] DSM/Irfu, CEA Saclay, 91191 Gif-Sur-Yvette Cedex, France
[23] Astronomical Observatory, The University of Warsaw, Al. Ujazdowskie 4, 00-478 Warsaw, Poland
[24] School of Physics, University of the Witwatersrand, 1 Jan Smuts Avenue, Braamfontein, 2050 Johannesburg, South Africa
[25] Landessternwarte, Universität Heidelberg, Königstuhl, 69117 Heidelberg, Germany
[26] Oskar Klein Centre, Department of Physics, Stockholm University, Albanova University Center, 10691 Stockholm, Sweden
[27] Wallenberg Academy Fellow
[28] Université Bordeaux 1, CNRS/IN2P3, Centre d'Études Nucléaires de Bordeaux Gradignan, 33175 Gradignan, France
[29] Funded by contract ERC-StG-259391 from the European Community
[30] School of Chemistry & Physics, University of Adelaide, 5005 Adelaide, Australia
[31] APC, AstroParticule et Cosmologie, Université Paris Diderot, CNRS/IN2P3, CEA/Irfu, Observatoire de Paris, Sorbonne Paris Cité, 10, rue Alice Domon et Léonie Duquet, 75205 Paris Cedex 13, France
[32] UJF-Grenoble 1/CNRS-INSU, Institut de Planétologie et d'Astrophysique de Grenoble (IPAG) UMR 5274, 38041 Grenoble, France
[33] Department of Physics and Astronomy, The University of Leicester, University Road, Leicester, LE1 7RH, UK
[34] Instytut Fizyki Jądrowej PAN, ul. Radzikowskiego 152, 31-342 Kraków, Poland
[35] Laboratoire Univers et Particules de Montpellier, Université Montpellier 2, CNRS/IN2P3, CC 72, Place Eugène Bataillon, 34095 Montpellier Cedex 5, France
[36] Laboratoire d'Annecy-le-Vieux de Physique des Particules, Université de Savoie, CNRS/IN2P3, 74941 Annecy-le-Vieux, France
[37] Obserwatorium Astronomiczne, Uniwersytet Jagielloński, ul. Orla 171, 30-244 Kraków, Poland
[38] Toruń Centre for Astronomy, Nicolaus Copernicus University, ul. Gagarina 11, 87-100 Toruń, Poland
[39] Department of Physics, University of the Free State, PO Box 339, 9300 Bloemfontein, South Africa
[40] Charles University, Faculty of Mathematics and Physics, Institute of Particle and Nuclear Physics, V Holešovičkách 2, 180 00 Prague 8, Czech Republic
[41] Laboratoire AIM, CEA-IRFU/CNRS/Université Paris Diderot, Service d'Astrophysique, CEA Saclay, 91191 Gif sur Yvette, France
[42] Dipartimento di Fisica "M. Merlin" dell'Università e del Politecnico di Bari, 70126 Bari, Italy
[43] Istituto Nazionale di Fisica Nucleare, Sezione di Bari, 70126 Bari, Italy
[44] Laboratoire de Physique et Chimie de l'Environnement, LPCE UMR 6115 CNRS, 54071 Orleans Cedex 02, and Station de radioastronomie de Nançay, Observatoire de Paris, CNRS/INSU, 18330 Nançay, France
[45] W. W. Hansen Experimental Physics Laboratory, Kavli Institute for Particle Astrophysics and Cosmology, Department of Physics and SLAC National Accelerator Laboratory, Stanford University, Stanford CA 94305, USA
[46] Max-Planck-Institut für Gravitationsphysik (Albert-Einstein-Institut), 30167 Hannover, Germany
[47] Leibniz Universität Hannover, 30167 Hannover, Germany
[48] Rikkyo University/Department of Physics, 3-34-1 Nishi-Ikebukuro, Toshima-ku, 171-8501 Tokyo, Japan